BNL-105172-2014-TECH

Booster Technical Note No. 128;BNL-105172-2014-IR

Effect of a wall impedance on the RF capture of a chopped beam in the AGS Booster

F. Z. Khiari

August 1988

Collider Accelerator Department

Brookhaven National Laboratory

U.S. Department of Energy

USDOE Office of Science (SC)

DISCLAIMER

EFFECT OF A WALL IMPEDANCE ON THE RF CAPTURE OF A CHOPPED BEAM IN THE AGS BOOSTER

AD

BOOSTER TECHNICAL NOTE

NO. 128

F. KHIARI, A. LUCCIO

AUGUST 22, 1988

ACCELERTOR DEVELOPMENT DEPARTMENT
BROOKHAVEN NATIONAL LABORATORY
UPTON, NEW YORK 11973

EFFECT OF A WALL IMPEDANCE ON THE RF CAPTURE OF A CHOPPED BEAM IN THE AGS BOOSTER

F.Z. Khiari and A.U. Luccio

Accelerator Development Department,

Brookhaven National Laboratory,

Upton, New York 11973

I Introduction

The AGS Booster is designed to rapidly accelerate high intensity beams ($1.5\ 10^{13}$) of protons to a kinetic energy of 1.5 GeV and inject them into the AGS. Due to the high beam currents present in the machine, even a small beam loss during the rf capture will result in unacceptably high background radiation around the accelerator ring. To avoid this problem, it is necessary to capture the maximum number of injected particles. In a previous note[1], we presented the results of a series of simulation studies of proton rf capture in the AGS Booster in the presence of space charge. We concluded from those studies that it was necessary to chop the incoming beam from the Linac in order to achieve a capture efficiency greater than 90%. To this effect, the computer code ESME[2] was further improved to simulate the capture process of a chopped beam. In this note, we report on a new series of simulation studies of proton rf capture in the AGS Booster for the case of a chopped beam in the presence of a wall impedance.

II RF Capture of a Chopped Beam with Space Charge[3]

We studied 6 cases which we will label 1, 2, 3, 4A, 4B, and 4C. All the cases were done for the voltage program shown in Fig. 1 and for an initial random uniform azimuthal

distribution and a gaussian energy distribution with $\sigma_E \approx 0.2\ MeV$ at an injection energy of 200 MeV for cases 1–4B and 201 MeV for case 4C. We found the voltage curve in Fig. 1 to be near optimum for both early capture and later acceleration. The magnetic field used in the different cases was given by

$$B(t) = B_i + (B_f - B_i)(\frac{t - t_i}{t_f - t_i})^{\alpha}, \tag{1}$$

where B_i =0.16 T and B_f =0.54 T are the initial and final magnetic fields defined at times $t_i = 0$ and $t_f = 60\ ms$ respectively. The coefficient α was equal to 2 for case 1, 3/2 for case 2, 5/4 for case 3, and 1 for cases 4A–4C. The curves of the magnetic field programs are shown in Fig. 2.

One first simulation was made for the case where we chopped 5° on each side of every bunch of the injected Linac beam (cases 1–4A). This amounts to $\approx$ 8% of the total beam delivered by the source. The bucket areas and rf captures for theses cases are listed in Table 1. Notice that the rf captures for cases 1, 2 and 3 are all high but the rf capture for case 4A is unacceptably small. This is due to the fact that $\dot{B}(t)$, given by

$$\dot{B}(t) = \alpha(B_f - B_i)\frac{t^{\alpha-1}}{t_f^{\alpha}} \tag{2}$$

starts from zero and increases more or less slowly therefrom for cases 1, 2 and 3 whereas it has a constant value of $\approx 6.4\ T/s$ during the whole cycle for case 4A. This makes the bucket area and the rf capture at injection for case 4A much smaller than those of cases 1, 2 and 3. To illustrate this, we show the particle distribution in phase–space and the rf bucket at the beginning of injection for cases 1–3 and 4A in Fig. 3a and Fig. 3b respectively. This demonstrates the fact that during capture, the rate of rise of the magnetic field should be kept as low as possible to be able to create the largest bucket area for a given initial voltage. With large $\dot{B}$, as for case 4A, chopping the beam loses its advantage since the bucket area is reduced due to the large value of $\dot{B}$.

To improve the rf capture for case 4A, we chopped more beam. We studied case 4B, shown in Fig. 4, where we chopped $\approx 30°$ on one side of each bunch of the injected beam and $\approx 17°$ on the other. This corresponds to $\approx 50\%$ of the total beam from the source. This, of course, has improved the rf capture ($\approx 80\%$), but not enough to bring it to the level of cases 1–3. The difference in this case can be accounted for by the bucket motion during the 100 μsec (≈ 84 turns) injection time. This motion is related to the energy gain per turn of the synchronous particle which is given by

$$\Delta E/Turn[MeV] = 2\pi\rho R\dot{B}10^{-6}, \tag{3}$$

where $\rho = 13.75\ m$ is the curvature radius of the Booster dipole magnets and $\breve{R} = 32.114\ m$ is the average radius of the equilibrium orbit. With $\dot{B} \approx 6.4\ T/s$, we get $\Delta E/Turn \approx 17.7\ kV$. Therefore, the bucket moves up in energy by about 1.5 MeV during the 84 turns it takes to finish injection.

Case 4C shows the effect of injection of the chopped Linac beam at 201 MeV kinetic energy instead of 200 MeV. We show in Fig. 5 the evolution of the beam–rf bucket system during the first 100 μsec of the multiturn injection for case 4C. This finally has made the rf capture at 500 μsec and 1 ms very close to that of cases 1–3 (see Table 1). However, the overall capture efficiency from the Linac drops from 92% to 50%, a price too high to be affordable.

III Wall Impedance Effects

In the capture studies presented so far, we included the rf focusing and the space charge forces only. Some studies have also been made to evaluate the contribution from the wall impedances. This wall impedance ($Z^W(\omega)$) combines with the space charge impedance ($Z^{sc}(\omega)$) to induce a voltage

$$V^i(\theta) = \sum_n Z(n\omega_{rf})I_n(\theta), \tag{4}$$

where $Z \equiv Z^{sc} + Z^W$ and $I_n(\theta)$ is the n^{th} complex Fourier component of the beam current

$$I_n(\theta) = eN\omega_{rf}a_n e^{i(n\theta+\theta_n)}. \tag{5}$$

N is the number of particles per bunch and a_n and θ_n are the real amplitude and phase of the n^{th} component of the spectrum of the beam current. The resulting energy change is then

$$\delta E(\theta) = \Re(eV^i(\theta)) = e^2 N\omega_{rf}\Re\sum_n [Z^W(n\omega_{rf}) + i\frac{nZ_\circ g}{2\beta\gamma^2}]a_n e^{i(n\theta+\theta_n)}, \tag{6}$$

where $\Re$ denotes the real part and we use the convention $i = -j$. Expressing Z^W as $\Re Z^W + i\Im Z^W$ we get

$$\delta E(\theta) = e^2 N\omega_{rf}\Re\sum_n \left[\Re Z^W(n\omega_{rf}) + i[\Im Z^W(n\omega_{rf}) + \frac{nZ_\circ g}{2\beta\gamma^2}]\right]a_n e^{i(n\theta+\theta_n)}. \tag{7}$$

Z^W can also be expressed as

$$Z^W = |Z^W|e^{i\chi}. \tag{8}$$

where χ is the wall impedance phase angle. The real and imaginary parts of Z^W are then given by

$$\Re Z^W = |Z^W|cos\chi, \tag{9}$$

and

$$\Im Z^W = |Z^W|sin\chi. \tag{10}$$

The energy change can then be expressed as

$$\delta E(\theta) = e^2 N\omega_{rf}\sum_n a_n|Z(n\omega_{rf})|cos(n\theta + \theta_n + \varphi_n), \tag{11}$$

where

$$|Z(n\omega_{rf})| = \sqrt{|Z^W(n\omega_{rf})|^2 cos^2\chi + \left[|Z^W(n\omega_{rf})|sin\chi + \frac{nZ_o g}{2\beta\gamma^2}\right]^2}, \qquad (12)$$

and

$$\varphi_n = tan^{-1}\frac{|Z^W(n\omega_{rf})|sin\chi + nZ_o g/2\beta\gamma^2}{|Z^W(n\omega_{rf})|cos\chi}. \qquad (13)$$

Elaborating on case 4C, we studied the rf capture for 5 additional cases in which we varied $|Z^W|$ and χ. We label these cases 5A–B and 6A–C and show in Fig. 7 a log–plot of the wall impedance used in the simulations. Since we bin the particles in 128 bins, we can only determine a maximum of 64 harmonics of the beam current. Therefore the beam harmonic number $n \equiv \omega/\omega_{rf}$ varies from 1 for the fundamental to 64 for the highest harmonic. Table 2 lists the various cases and their respective rf capture efficiencies at selected times during the early part of the cycle. Notice that the wall impedance for cases 5A and 5B ($|Z^W| = 200\ \Omega$, n = 1–6; $|Z^W|$ is higher for higher beam harmonics) does not affect the rf capture. The space charge contribution is still the dominant one. However, the wall impedance for cases 6A–6C ($|Z^W| = 20\ k\Omega$, n = 1–6) does have an effect on the rf capture and this effect depends on the value of the angle χ. Notice then that when $\chi = \pi/2$, the imaginary parts of the wall impedance and the space charge impedance add and their combined effect on the rf capture is strongest. There is 10% loss due to the wall impedance in this case. In contrast, when $\chi = -\pi/2$, the imaginary parts of the space charge impedance and the wall impedance have opposite signs and their combined effect on the rf capture is weakest. In this case the maximum rf capture is comparable to the maximum rf capture in the absence of the wall impedance. The rf capture for case 6B is plotted in Fig. 8. The oscillations in the rf capture are attributed to bunch oscillations inside the rf bucket as illustrated in Fig. 9. The mechanism behind these oscillations is not yet understood and needs further investigation. As expected, the rf capture for case

6C where $\chi = 0$ lies somewhere between those of the previous two cases. In fact there is a 5% loss in this case.

To further illustrate the effect of the impedance phase angle χ on the rf capture, we list in Table 3 the value of

$$\sqrt{<(\delta E)^2>} = \sqrt{\frac{1}{2\pi}\int_0^{2\pi}[\delta E(\theta)]^2 d\theta} \tag{14}$$

for cases 4C and 6A–C. As expected, $\sqrt{<(\delta E)^2>}$ is smallest for $\chi = -\pi/2$. However, even though the peak induced voltage is highest for $\chi = \pi/2$ (causing more beam loss), the oscillations in δE from bin to bin are more numerous for $\chi = 0$ thereby causing $\sqrt{<(\delta E)^2>}$ to be largest for this last case.

IV Conclusions and discussions

From the studies presented in this note, some conclusions can be drawn:

1. By chopping the Linac beam, we eliminate those particles that are close to the unstable fixed point of the rf bucket which results in a higher capture.

2. The case with a chopped beam and a slow magnetic field rise during capture (cases 1–3) gives a better capture efficiency because the bucket area is maximum for the voltage at injection.

3. The broad band wall impedance starts to affect the rf capture at $|Z^W|/n \geq 3\ k\Omega$, but there is a noticeable dependence of the rf capture on the phase angle of the wall impedance with respect to the phase angle of the space charge impedance. When these two angles are opposite to each other, the bunches oscillate inside the rf buckets causing the rf capture to oscillate. The highest losses (10%) occur when the wall impedance and the space charge impedance have equal phase angles. The losses are reduced to 5% when these two impedances are at 90° with respect each other.

REFERENCES

[1] F. Z. Khiari, A. U. Luccio, W. T. Weng, *ESME at BNL: Status Report and Simulation study of Proton rf Capture in the BNL Booster* AD Booster Technical Note No. 118 (1988).

[2] J. A. MacLachlan, *Particle Tracking in E-ϕ Space as a Design Tool for Cyclic Accelerators*, Proceedings of The IEEE Particle Accelerator Conference, 1087 (1987).

[3] F. Z. Khiari, A. U. Luccio, W. T. Weng, *Simulation of Proton RF capture in the AGS Booster*, BNL 41462.

Case #	α	500 μsec	1 ms
1	2	1.6/100	-
2	1.5	1.6/100	1.5/99
3	1.25	1.4/96	1.4/96
4A	1	1.1/55	-
4B	1	1.1/82	1.1/82
4C	1	1.1/98	1.1/98

Table 1. List of Bucket Area[$eV.sec$]/Capture[%] for cases 1–4C

Case #	4C	5A	5B	6B	6C	6A
$\|Z^W\|[k\Omega]$	0	0.2	0.2	20	20	20
χ [rad]	-	$-\pi/2$	$\pi/2$	$-\pi/2$	0	$\pi/2$
			Capture [%]			
0 μsec	59	59	59	59	59	59
50	75	75	75	76	74	73
100	84	84	84	86	86	78
150	98	98	98	96	94	88
200	99	99	99	97	95	88
300	98	98	98	98	95	88
500	98	98	98	92	94	89
1 $msec$	98	98	98	97	93	88

Table 2. List of Wall Impedances and RF Captures for Cases 4C, 5A–B and 6A–C.

Case #	4C	6B	6C	6A
		$\sqrt{<(\delta E)^2>}[keV]$		
100 μsec	6	0.01	29	7
500	7	0.02	32	8
1 $msec$	6	0.02	32	11

Table 3. List of $\sqrt{<(\delta E)^2>}$ for cases 4C and 6A–C.

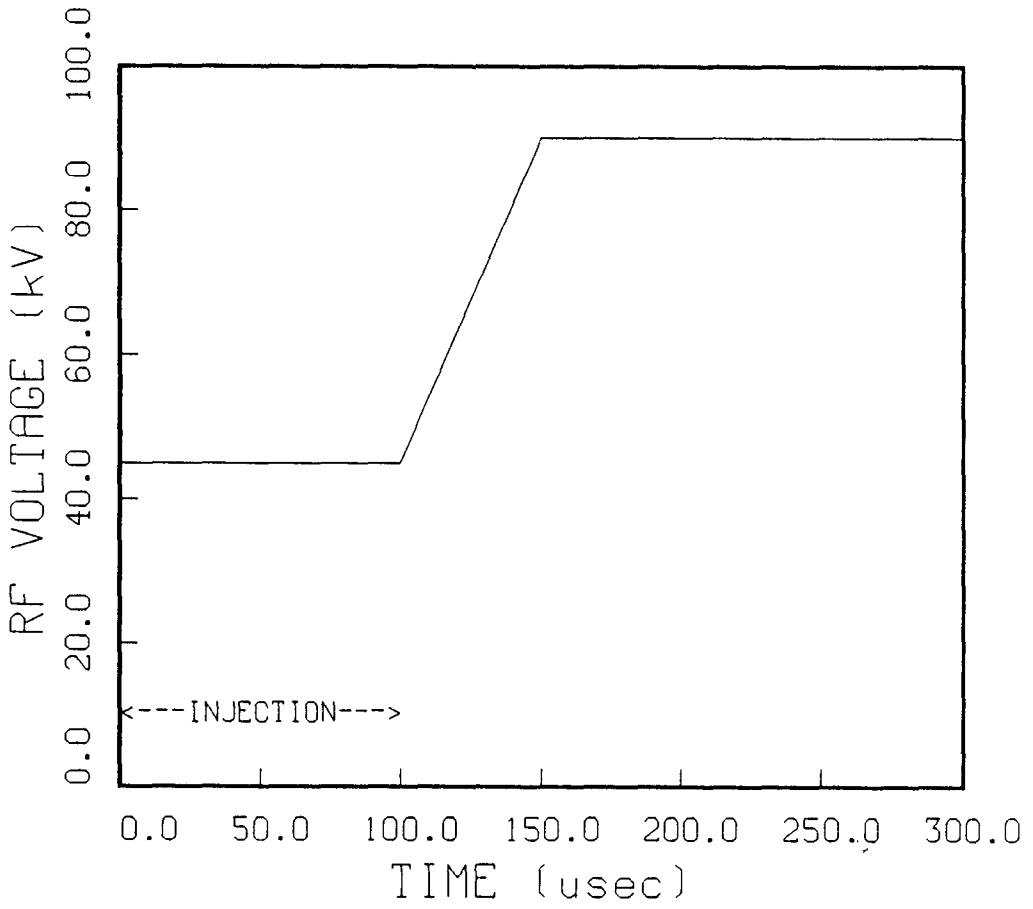

Fig. 1. RF VOLTAGE PROGRAM FOR CASES 1, 2, 3 and 4.A--4.C

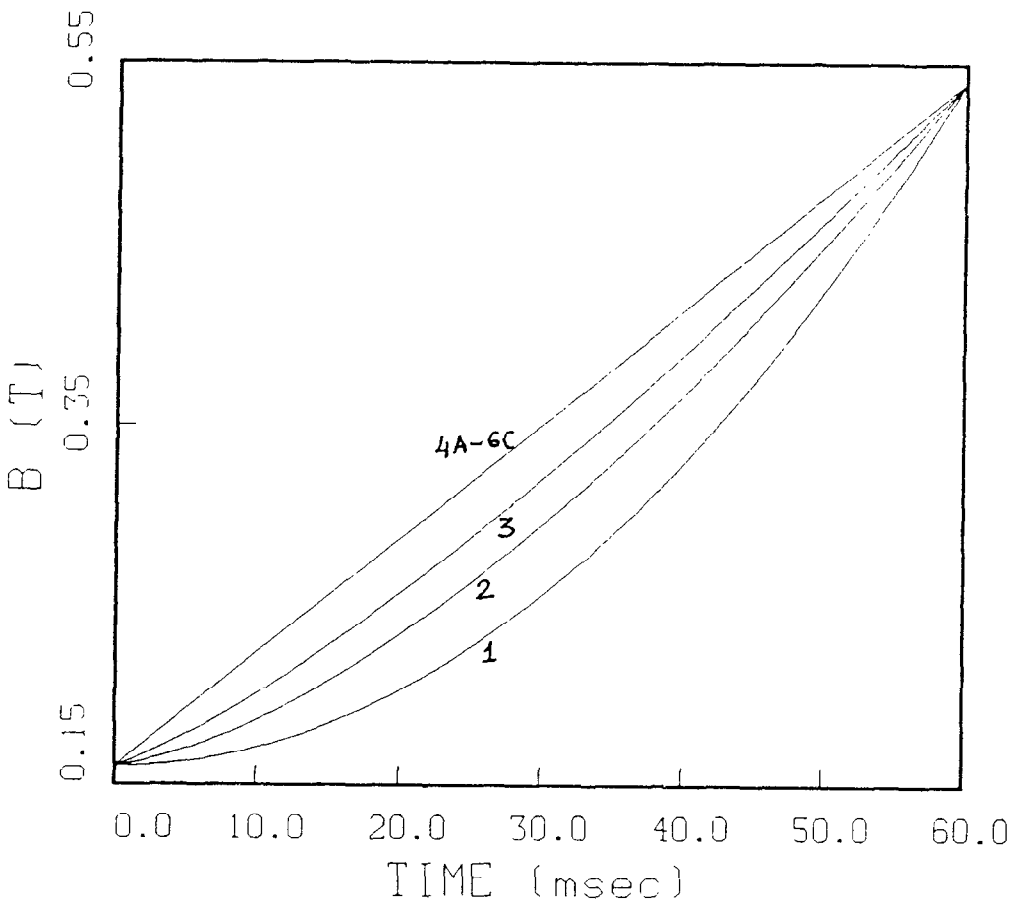

Fig. 2 B Curves for Cases 1–3 and 4A–6C

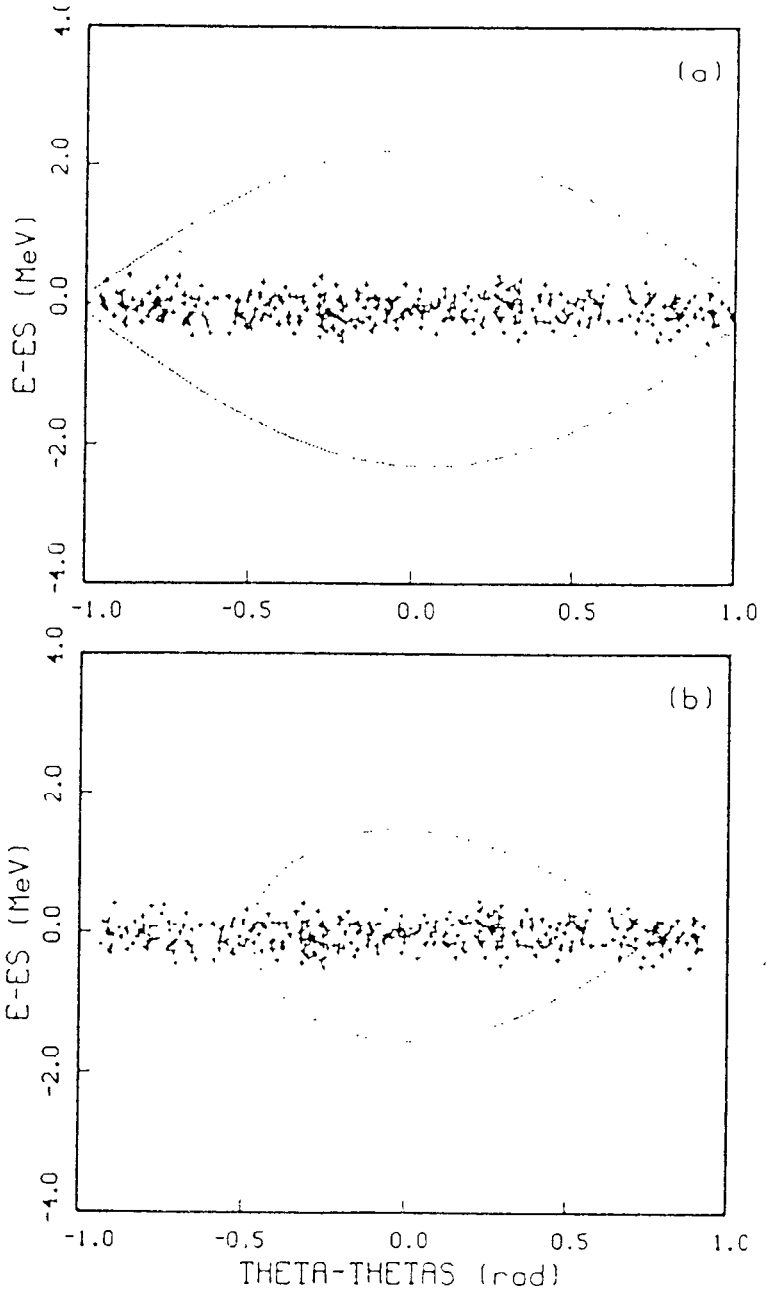

Fig. 3. a) Initial distribution and rf bucket for cases 1–3.
b) Case 4.A.

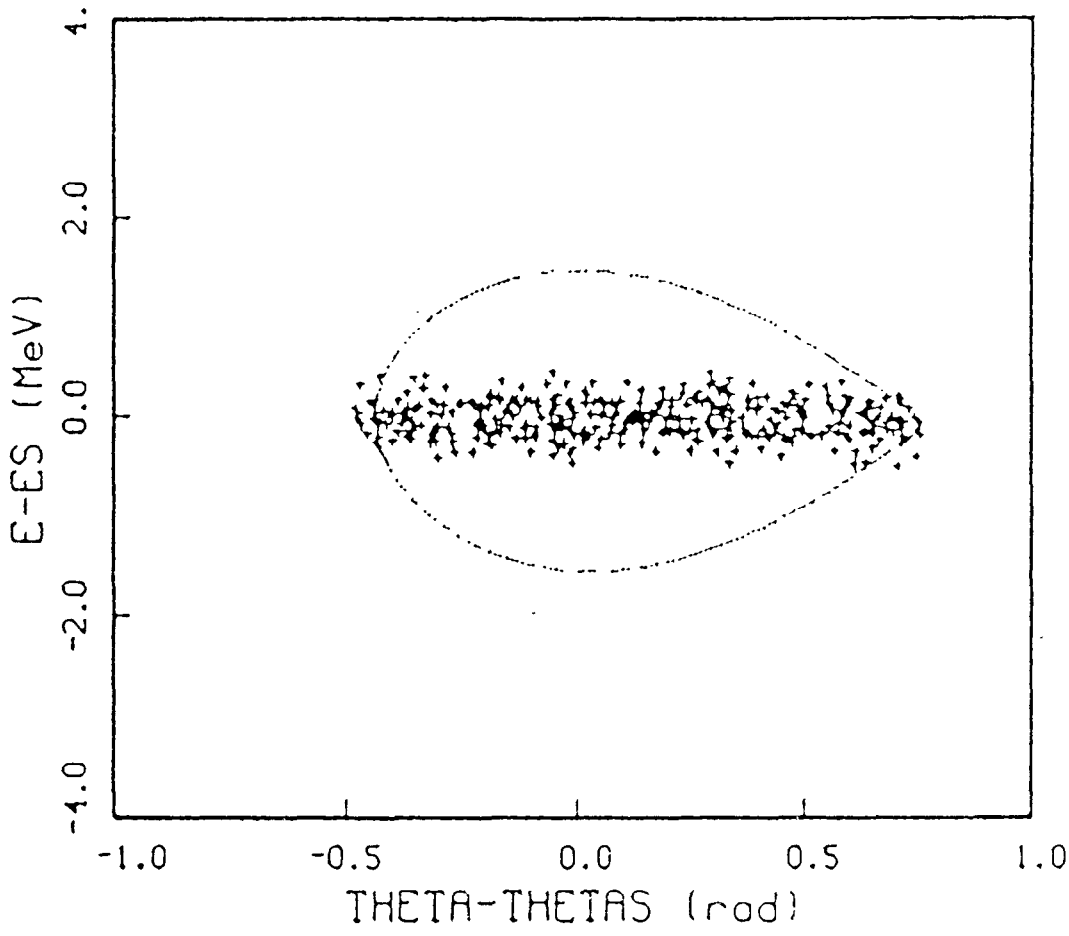

Fig. 4. Initial distribution and rf bucket for case 4.B.

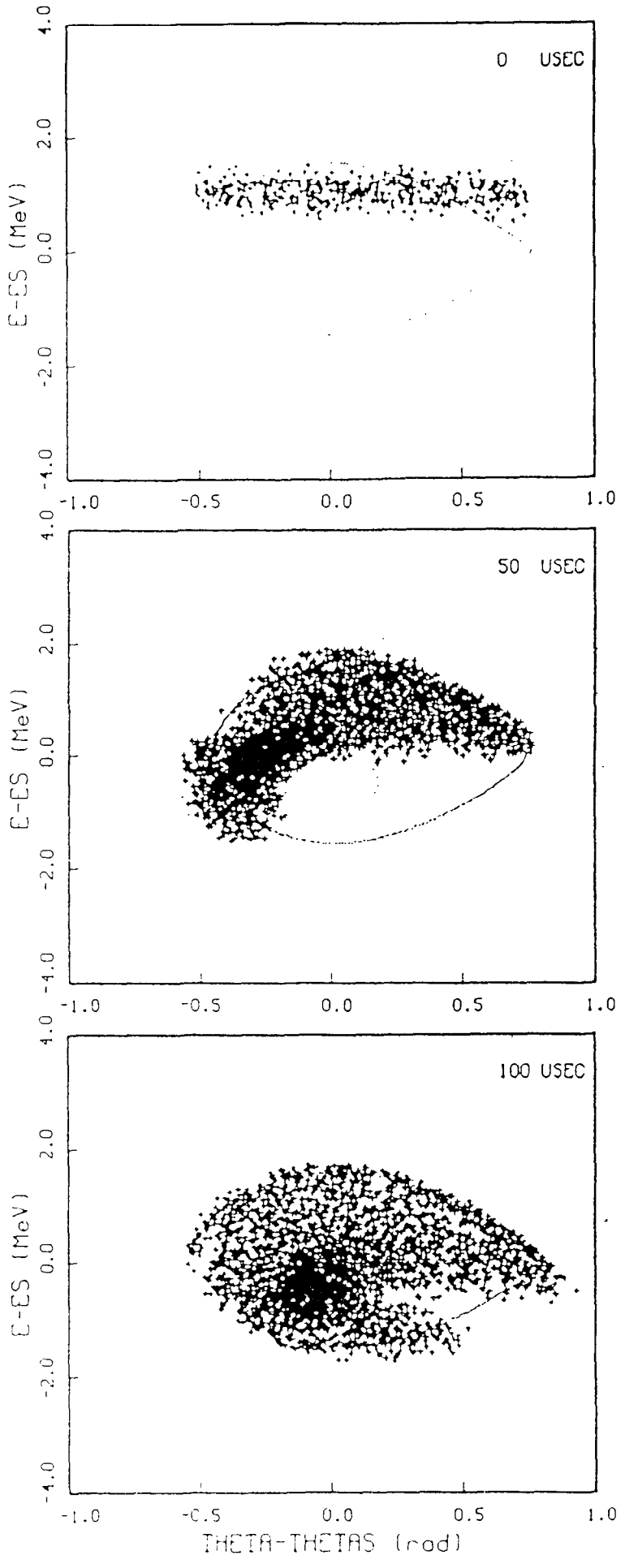

Fig. 5. Distribution for case 4.C at 0, 50, and 100 μsec.

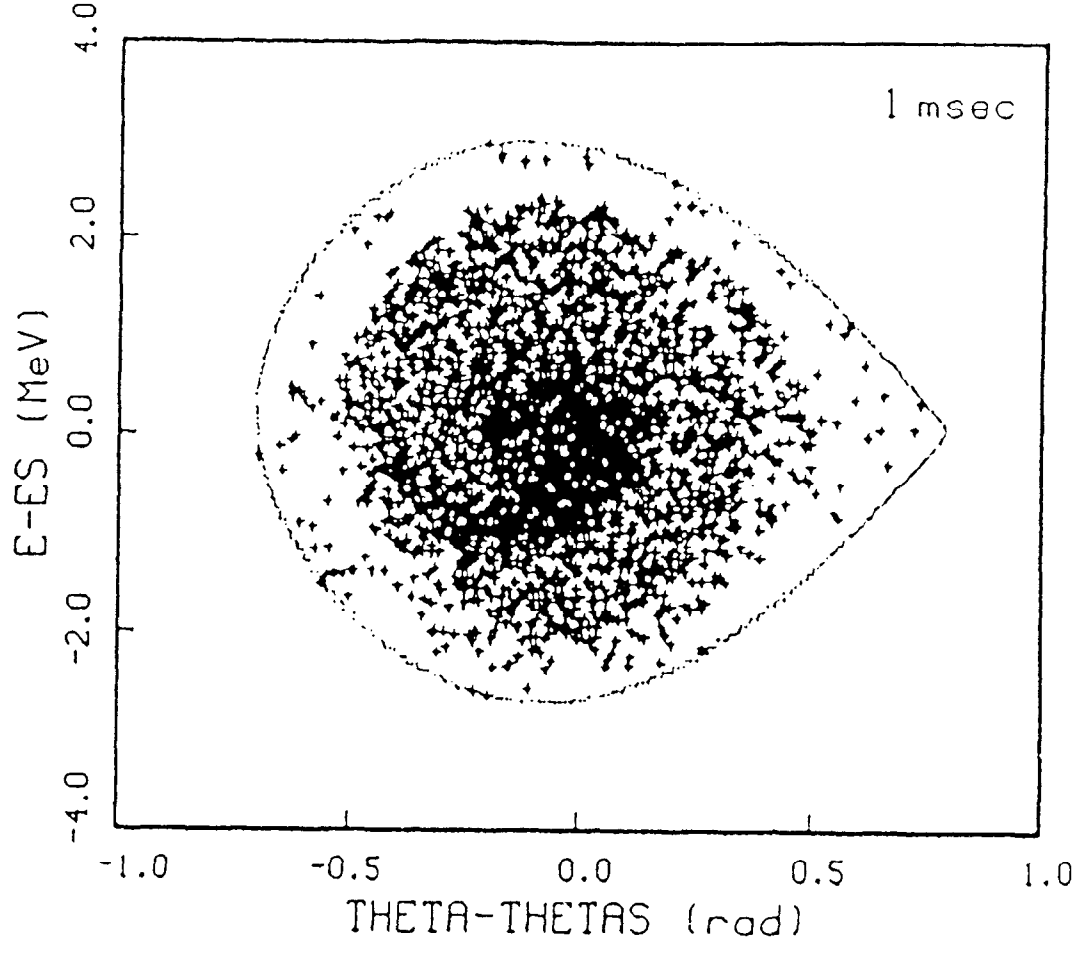

Fig. 6. Proton beam captured in the rf bucket at 1 *msec.* for case 4.C.

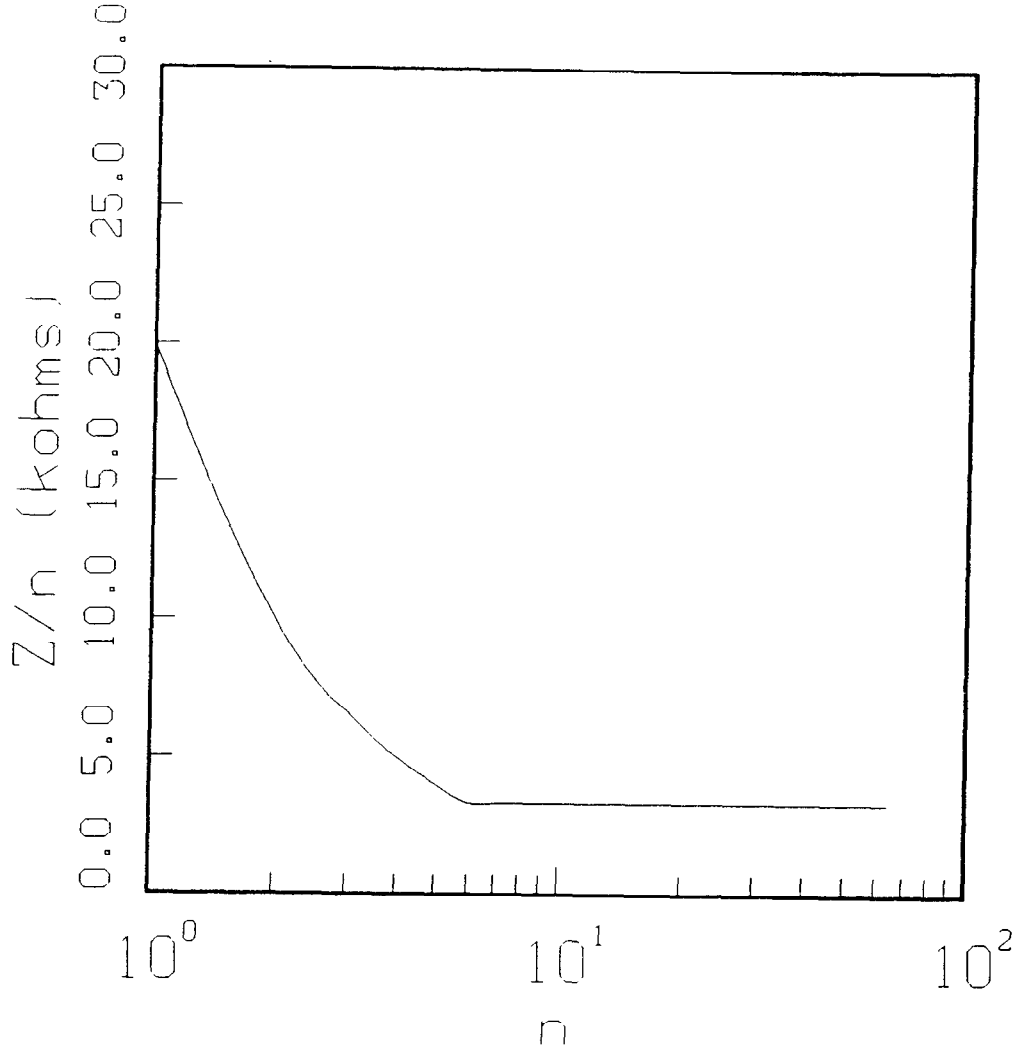

Fig. 7 Wall Impedance used in the Simulations of Cases 6A–6C

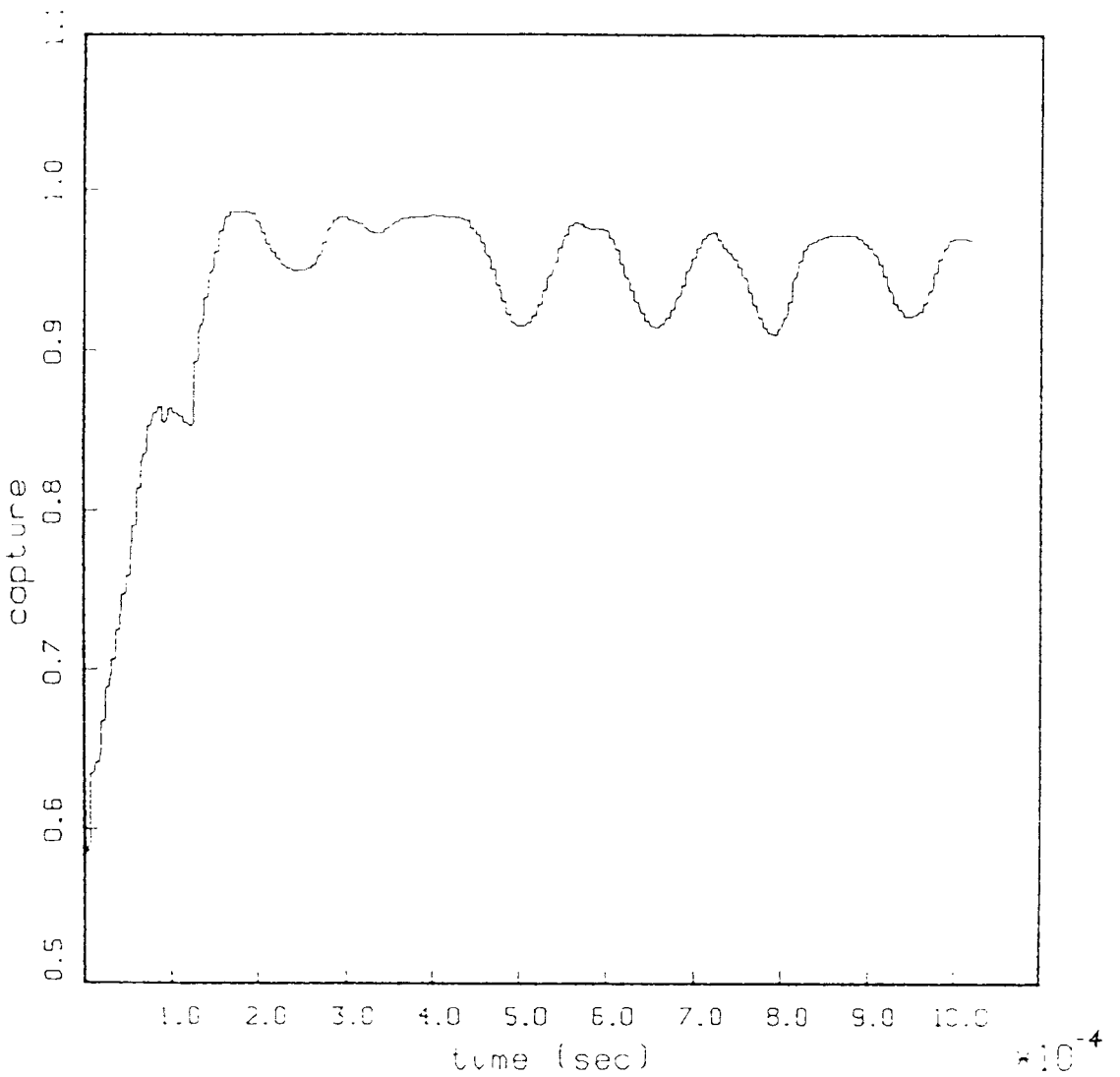

Fig. 8 Plot of the RF Capture for Case 6B ($\chi = 0$)

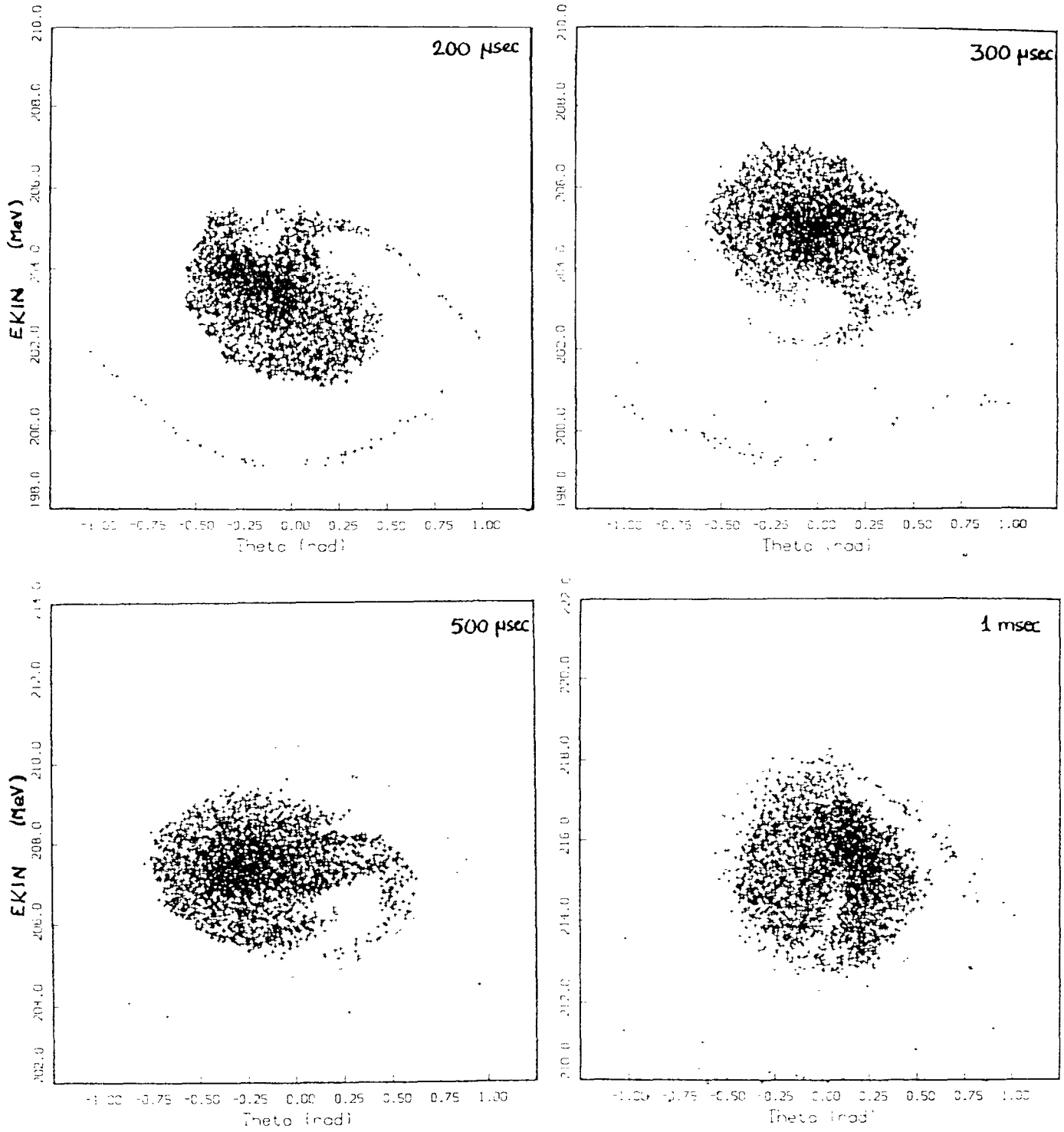

Fig. 9 Phase Space Plots for Case 6B showing the Bunch Oscillations inside the RF Bucket